# Concurrent Asian monsoon strengthening and early modern human dispersal to East Asia during the last interglacial

Hong Ao, Jiaoyang Ruan, María Martinón-Torres, Mario Krapp, Diederik Liebrand, Mark J Dekkers, Thibaut Caley, Tara N Jonell, Zongmin Zhu, Chunju Huang, et al.

# Concurrent Asian monsoon strengthening and early modern human dispersal to East Asia during the last interglacial

Hong Ao[a, b]*, Jiaoyang Ruan[c, d]*, María Martinón-Torres[e, f], Mario Krapp[g], Diederik Liebrand[h], Mark J. Dekkers[i], Thibaut Caley[j], Tara N. Jonell[k], Zongmin Zhu[l], Chunju Huang[l], Xinxia Li[l], Ziyun Zhang[m], Qiang Sun[n], Pinguo Yang[l], Jiali Jiang[l], Xinzhou Li[a], Xiaoxun Xie[a], Yougui Song[a], Xiaoke Qiang[a], Peng Zhang[a], Zhisheng An[a,b]

[a]State Key Laboratory of Loess and Quaternary Geology, Institute of Earth Environment, Chinese Academy of Sciences, Xi'an, China

[b]Laoshan Laboratory, Qingdao, China

[c]Center for Climate Physics, Institute for Basic Science, Busan, South Korea

[d]Pusan National University, Busan, South Korea

[e]National Research Center on Human Evolution, Burgos, Spain

[f]Department of Anthropology, University College London, London, UK

[g]Department of Zoology, University of Cambridge, Cambridge, UK

[h]Department of Earth and Environmental Sciences, The University of Manchester, Manchester, UK

[i]Palaeomagnetic Laboratory 'Fort Hoofddijk', Department of Earth Sciences, Faculty of Geosciences, Utrecht University, Utrecht, The Netherlands

[j]Univ. Bordeaux, CNRS, Bordeaux INP, EPOC, UMR 5805, F-33600 Pessac, France

[k]School of Geographical and Earth Sciences, University of Glasgow, Glasgow, UK

[l]School of Earth Sciences, China University of Geosciences (Wuhan), Wuhan, China

[m]College of Life Science, Shanxi Normal University, Taiyuan, China

[n]College of Geology and Environment, Xi'an University of Science and Technology, Xi'an, China

*Corresponding author: aohong@ieecas.cn (H. Ao); jiaoyangruan@pusan.ac.kr (J. Ruan)

**Classification:**

Major classification: Earth, Atmospheric, and Planetary Sciences

Minor classification: Geology

**Keywords:** Asian monsoon; paleoclimate; loess; environmental magnetism; human dispersal

**This PDF file includes:**

Main Text

Captions of Figures 1 to 4

## Abstract

**The relationship between initial *Homo sapiens* dispersal from Africa to East Asia and the orbitally paced evolution of the Asian summer monsoon (ASM)—currently the largest monsoon system—remains underexplored due to lack of coordinated synthesis of both Asian paleoanthropological and paleoclimatic data. Here we investigate orbital-scale ASM dynamics during the last 280 thousand years (kyr) and their likely influences on early *H. sapiens* dispersal to East Asia, through a unique integration of (*i*) new centennial-resolution ASM records from the Chinese Loess Plateau, (*ii*) model-based East Asian hydroclimatic reconstructions, (*iii*) paleoanthropological data compilations, and (*iv*) global *H. sapiens* habitat suitability simulations. Our combined proxy- and model-based reconstructions suggest that ASM precipitation responded to a combination of Northern Hemisphere ice volume, greenhouse gas, and regional summer insolation forcing, with co-occurring primary orbital cycles of ~100-kyr, 41-kyr, and ~20-kyr. Between ~125 and 70 kyr ago, summer monsoon rains and temperatures increased in vast areas across Asia. This episode coincides with the earliest *H. sapiens* fossil occurrence at multiple localities in East Asia. Following the transcontinental increase in simulated habitat suitability, we suggest that ASM strengthening together with Southeast African climate deterioration may have promoted the initial *H. sapiens* dispersal from their African homeland to remote East Asia during the last interglacial.**

## Significance Statement

The precise role of climate shifts in early human dispersal to East Asia is important in paleoclimatology and paleoanthropology. Our proxy- and model-integrated paleoclimate reconstructions for the last 280 thousand years reveal a dynamic response of Asian summer monsoon variability to the combined effects of orbital-scale insolation, Northern Hemisphere ice volume, and greenhouse gas changes. By comparing paleoclimate data with a new compilation of *H. sapiens* fossil and archaeological finds from Asia and simulated global *H. sapiens* habitat suitability, we show that orbitally-modulated summer monsoon rainfall and temperature increases in East Asia and Southeast African climate deterioration may have promoted the early *H. sapiens* dispersal out of Africa, to the more remote region(s) of East Asia, during the last interglacial.

## Main Text

Anatomically modern human (AMH), or *Homo sapiens*, emerged in Africa at least 200–300 thousand years ago (ka) (1, 2). Integrated paleoclimatic and paleoanthropological data have shown that orbital-scale regional climate variability played a key role in driving AMH dispersal within Africa and to adjacent Middle East (3-7). However, such integrated investigations remain sparse for South and East Asia, despite spanning a much larger areal extent and wider range of climatic and biographical zones than Africa, and hosting multiple important *H. sapiens* fossils dated back to ~100 ka (8-10) (Fig. 1). Moreover, South and East Asia serve as a land conduit through which AMH dispersed from Africa to Australia, Polynesia, and ultimately the Americas (8, 9) (Fig. 1). Thus, understanding *H. sapiens* fossils and archaeological finds in appropriate paleoclimatic context is essential to developing a global perspective on AMH evolution and dispersal beyond Africa.

The Asian summer monsoon (ASM), comprising of the South (Indian) and East Asian sub-monsoon systems, governs moisture supply across low-latitude regions like the African monsoon, as well as to Asian latitudes as high as ~50°N, as is observed in northeastern China (Fig. 1). This far-reaching areal extent, and hence, climatic impact of the ASM, is globally unique. After decades of proxy and modeling research, however, ASM dynamics and its orbital-scale variations remain a subject of scientific debate (11-22). Furthermore, the precise role of orbital ASM dynamics on early *H. sapiens* dispersal to East Asia is an important topic in both paleoclimatological and paleoanthropological research, yet our understanding of it remains limited due to the scarcity of integrated ASM and paleoanthropological studies.

Here we develop new insight into the climatic influence on the dispersal of AMH to East Asia and orbital-scale ASM dynamics during the last 280 thousand years (kyr). Firstly, we study orbital-scale ASM dynamics by combining new centennial-resolution environmental magnetic records from the central Chinese Loess Plateau (CLP) with model-based continuous East Asian hydroclimate reconstructions (23) for the last 280 kyr. Secondly, we integrate proxy- and model-based spatiotemporal paleoclimatic reconstructions with Asian paleoanthropological and hydroclimatic data compilations and global *H. sapiens* habitat suitability simulations. We find that settling and dispersal conditions were optimal for the initial wave of AMH dispersal to East Asia during the last interglacial, when the stronger summer monsoon caused warmer and more humid conditions, while the coeval Southeast African conditions became less favorable.

**New ASM records from the CLP.** The CLP (~640,000 $km^2$) extends longitudinally from ~100 to 115°E and latitudinally from ~34 to 41°N (Fig. S1). The present-day climate on the CLP is dominated by seasonally-alternating southeasterly summer and northwesterly winter monsoon changes (22, 24, 25) (Fig. S1). The southeasterly wind penetration inland from tropical oceans (Fig. 1) produces summer time (May–September) rain that accounts for ~60–75% of the annual total (22, 24). Materials forming CLP loess-paleosol deposits are transported predominantly by near-surface winter monsoon winds from upstream arid northwestern China (25-27). Within the loess package, the extent of soil formation depends on moisture availability that is governed by the ASM. Thus, the CLP loess-paleosol deposits were widely used for paleo-monsoon reconstructions (12, 22, 24-26, 28).

Our study site, the Huanxian loess-paleosol section (107°15′E, 36°37′N), is located on the central CLP and sensitive to ASM penetration (Fig. S1). In this section, the loess-paleosol sequence

accumulated rapidly, with a sedimentation rate twice that of the classical sections located to the south and east. This enables investigation of the orbital-scale ASM variability at the Huanxian section in greater detail than typical. To measure ASM proxies in the laboratory, including magnetic susceptibility ($\chi$) and anhysteretic remanent magnetization (ARM), we collected in the field 2,066 samples from the 44 m thick strata, which covers from Holocene paleosol $S_0$ to mid-Pleistocene loess $L_3$, ranging between marine isotope stage (MIS) 1 and MIS 8, at 2–2.5 cm intervals (equivalent to a temporal resolution of ~0.1–0.8 kyr). Our age model reconstruction for the Huanxian loess-paleosol section consists of two steps (cf. Methods and Fig. S2). First, an initial age model was constructed through a detailed cycle-based correlation of $\chi$ with a globally averaged marine benthic foraminiferal $\delta^{18}O$ stack. Second, our final age model was based on a further, even more precise alignment, of our initial Huanxian loess-paleosol chronology to precisely U/Th-dated speleothem $\delta^{18}O$ records from East China (15). Support for our chronology construction comes independently from recent optically stimulated luminescence dating (29) (Fig. S2D).

Rock magnetic analyses suggest that the Huanxian loess-paleosol magnetic properties are dominated by fine-grained magnetite/maghemite particles (Figs. S3–S7; Supplementary Text 1). Enhanced pedogenesis within the sediment column under wetter climate accelerates formation of fine magnetite/maghemite particles, leading to higher $\chi$ and ARM values, and vice versa (24, 25). Therefore, the CLP loess-paleosol $\chi$ and ARM records are closely linked to the ASM precipitation. The lithological, $\chi$, and ARM records from the Huanxian loess-paleosol section vary consistently over the last 280 kyr (Fig. 2A–C). Paleosol layers (i.e., $S_0$, $S_1$, and $S_2$) have higher $\chi$ and ARM values than loess layers (i.e., $L_1$, $L_2$, and $L_3$), which is consistent with higher ASM precipitation during interglacials relative to glacials. The Huanxian $\chi$ and ARM records are marked by more square-wave ~100-kyr cycles, which

differ slightly from the asymmetric glacial-interglacial structure in the global reference sea level/ice volume record (30) (Fig. 2B–D). In addition to the ~100-kyr periodicity, Huanxian χ and ARM records are superimposed with lower-amplitude precessional (~20-kyr) variability, indicative of a possible low-latitude forcing linked to Northern Hemisphere summer insolation (NHSI). During MIS 5 and MIS 7, the superimposed precession-paced stadial substages occur close to NHSI minima and are not as dry as full glacial periods. During MIS 3–4 and early MIS 6, when glacial conditions were modest, somewhat moister interstadials occurred around NHSI maxima, albeit not as moist as interglacial periods (MIS 5 and MIS 7). However, during MIS 2–3, late MIS 6, and MIS 8, when glacial conditions were more extreme, aridity prevailed despite NHSI maxima. Spectral analyses of χ and ARM records confirm pervasive orbital cycles of eccentricity (~100-kyr), obliquity (41-kyr), and precession (~20-kyr), which are broadly comparable to the combined spectral results from NHSI, global average sea level, and atmospheric $CO_2$ records (30-32) (Fig. 2B–E). The NHSI is characterized by a precessional cyclicity, whereas globally averaged sea level and atmospheric $CO_2$ records are dominated by a strong ~100-kyr eccentricity-paced cyclicity, with subdued expressions of obliquity- and precession-paced cycles.

**Dynamics of orbital-scale ASM variability.** The co-occurring primary orbital cycles of ~100-kyr, 41-kyr, and ~20-kyr in the Huanxian loess-paleosol sequence cannot solely be explained by either an external (insolation) or internal (ice volume and greenhouse gas concentration) driver, but more likely through their combined action. Such an interpretation is further supported by a high-fidelity paleoclimate simulation, in which we utilized the climate output from a general circulation model forced by a combination of orbital-scale insolation, global ice volume, and atmospheric $CO_2$ forcing factors (model details are provided in reference (23)). Model-based reconstructions of (*i*) annual and summer (May to September) precipitation over North (100–120°E; 30–45°N) and South China (100–120°E; 20–30°N), (*ii*)

low-latitude East Asian (100–120°E, 20°N) summer temperature, (*iii*) summer precipitable moisture on the West Pacific and North Indian oceans (80–150°E; 0–35°N), and (*iv*) summer wind speed show broadly similar orbital variability as our proxy records during the last 280 kyr, with combined eccentricity, obliquity, and precession cycles (Fig. 2). Therefore, both proxy- and model-based reconstructions support that the NHSI, ice volume, and greenhouse gas concentration jointly governs East Asian summer precipitation (12, 21, 22, 33).

In contrast to Huanxian records, precession signal is largely subdued or absent in many χ records located to the south and east (Figs. S1 and S8). However, like Huanxian records, precessional variability is prominent in the Jingyuan carbonate $\delta^{13}C$ record (22) and the Xijing spliced grain size-χ stack from the western CLP (20) and the Baoji $^{10}Be$-based precipitation reconstruction from the southern CLP margin (12) (Fig. S9). Thus, faint or absent precessional variability in those southern/eastern CLP loess-paleosol sections, which are usually associated with lower sedimentation rates, does not necessarily mean that CLP precipitation responded negligibly to precession-paced NHSI changes. Our Huanxian hydroclimatic records, together with the Jingyuan, Xijing, and Baoji hydroclimatic records (12, 20, 22), reveal a widespread presence of precessional ASM variability across the entire CLP, beyond the western sections or the southern CLP margin as recently recognized (12, 20, 22) (Fig. S9). The distinct precession signal identified here, a typical monsoon pacing feature related to low-to-middle latitude insolation forcing (15, 16), together with our detailed rock magnetic results (Figs. S3–S7; Supplementary Text 1), supports the notion that the classical use of loess-paleosol χ as an ASM indicator (24, 25) is also (largely) valid for high sedimentation rate sections from the central CLP marked by higher ASM precipitation than the western CLP. However, secondary influences of pedogenic duration and temperature on χ cannot be fully excluded (20).

The precession signal in the Baoji $^{10}$Be record is not as obvious as that seen in Huanxian, Jingyuan, and Xijing ASM records (Fig. S9), which is possibly due to a lower sedimentation rate and data resolution as well as prominent gaps within MIS 5 and MIS 7. The Huanxian, Jingyuan, and Baoji records have a stronger ~100-kyr cyclicity than the Xijing record. These nuanced differences likely reflect variable responses of proxies to the extent of ASM precipitation. The Huanxian environmental magnetic records may be more directly related to regional ASM precipitation than the Jingyuan carbonate $\delta^{13}$C record and Xijing spliced grain size-$\chi$ stack. Jingyuan carbonate $\delta^{13}$C reflects local vegetation conditions likely linked to the complex interactions of precipitation, temperature, and $CO_2$ (20, 22). The Xijing spliced grain size-$\chi$ stack contains not only ASM precipitation-induced $\chi$ variations, but also winter monsoon-related grain size changes (25-27).

To better document the ASM history across the entire CLP and minimize the limitations of specific proxy records, we compile a new ASM stack by summing the Huanxian $\chi$ and ARM records, the Jingyuan carbonate $\delta^{13}$C record (22), the Xijing spliced grain size-$\chi$ stack (20), and the Baoji $^{10}$Be record (12) (Fig. S9). This new ASM stack shows consistency with East China composite speleothem $\delta^{18}$O records (15) in portraying the precessional variability, although our ASM stack contains additionally ~100-kyr and 41-kyr cycles that are not distinct in the speleothem $\delta^{18}$O records (Fig. 3A–B). Nevertheless, co-occurring ~100-kyr, 41-kyr, and ~20-kyr periodicities have been captured by the Xiaobailong Cave $\delta^{18}$O record from Southwest China (13), the $\delta^{18}$O and $\delta D_{wax}$ records from the Indian margin U1446 sediment core (17, 18), and the Arabian Sea summer monsoon stack (14) (Fig. 3). These records together provide an important Asian climatic context for AMH dispersal from Africa to East Asia.

**Climatic influence on initial AMH dispersal to East Asia.** Multiple lines of fossil, archeological, and genetic evidence suggest that initial AMH arrivals in East Asia can be traced back to the last interglacial (more broadly MIS 5). Early Late Pleistocene sites with robust chrono-stratigraphic contexts and fossils that can be reasonably attributed to *H. sapiens* include localities such as Luna Cave (120–70 ka) (34), Zhiren Cave (113–100 ka) (35), and Fuyan Cave (120–80 ka) (36), that all range from ~130 ka to ~70 ka (Fig. 4A). Although a recent dating study on the Luna and Fuyan sites argued for younger ages (37), the two follow-up studies criticized these younger ages by raising important flaws in its sampling procedures and species attributions, thereby suggesting that MIS 5 fossil ages remained feasible (38, 39); an interpretation we support. Similarly old hominin fossils tentatively attributed to *H. sapiens* were also reported from Tongtianyan Cave (Liujiang, 130–70 ka) (40) and Ganqian Cave (140–100 ka) (41). Hominin fossils from Jimuyan (42), Dingcun (43), and Salawusu (43-45) have *H. sapiens* features, even though some primitive features in combination with larger age uncertainties make the interpretation of these fossils, in terms of AMH dispersal timing, relatively less unequivocal (43, 46). Likewise, two complete crania with closer affinities to *H. sapiens* but also some archaic features were reported from Ryonggok, North Korea (47, 48). Despite the fact that older ages were initially proposed for this finding, a younger age of 46–49 ka is currently more accepted (47, 48). The teeth from Lida Ajer Cave, Sumatra (73–63 ka) (49), suggests that AMH reached the island by ~70 ka. However, before settling in Sumatra, AMH must already have crossed mainland Southeast Asia (Fig. 1). Recently this was confirmed by the *H. sapiens* presence at Tam Pà Ling (Northern Laos) between 86 ka and 68 ka (50) (Fig. 1). Moreover, the 65-ka-old sophisticated toolkit found in North Australia indicate that AMH possibly crossed Southeast Asian islands during late MIS 5 when regional climate remained favorable and sea level started to decline (8, 51). The AMH presence in Asia during MIS 5 is supported not only by a large number of

geo-chronologically dated fossils and artifacts (Figs. 1 and 4A; Table S1) but also by independent genetic studies (52, 53) that suggest the Asian presence of modern human lineages earlier than 75 ka. Lastly, it is additionally supported by a recent finding that a deeply divergent modern humans contributed genetically to the ancestry of Altai Neanderthals by roughly 100 ka (53). We are cognizant of the inherent dating uncertainties associated with a few hominin sites and the debate regarding their species attribution (54, 55), so we do not attempt to distinguish AMH dispersal time to either the earlier or later part of MIS 5. Nevertheless, the available data confirm initial AMH arrivals in East Asia by the last interglacial (8).

The AMH occupation in MIS 5 East Asia (Fig. 4A) coincided with regional rain and temperature increases as seen in our proxy- and model-based reconstructions and existing paleoclimatic records from Asia (Figs. 2 and 3). To further examine ASM climate influence on AMH dispersal, we analyze *H. sapiens* habitats from a recently established transient Pleistocene simulation of this kind (7). This multi-dimensional statistical model simulates the habitat suitability for *H. sapiens* occupation at a given location and time, by quantifying the relationships among geo-chronologically dated fossil/archaeological data and different climatic variables of biological importance, i.e., yearly precipitation minimum, annual mean precipitation, temperature, and net primary productivity (7). The simulated *H. sapiens* habitat suitability over East Asia (80–130°E; 20–55°N) shows large temporal variation during the last 280 kyr (Fig. 4B), with both ~100-kyr and ~20-kyr cyclicities comparable to the aforementioned Asian hydroclimatic oscillations (Figs. 2 and 3). Interestingly, the temporal increases in simulated East Asian *H. sapiens* habitat peaked at ~120 ka, ~95 ka, and ~70 ka, in comparison to the preceding glacial MIS 6 (Fig. 4B). This is coeval with the orbitally-modulated ASM strengthening (Figs. 2 and 3) and the earliest AMH fossil occurrences in East Asia (Fig. 4A; Table S1). We argue that the ASM strengthening in MIS 5

induced (*i*) regional precipitation increases (Figs. 2 and 3), (*ii*) a greener, more lushly vegetated East Asia, and (*iii*) more abundant food resources, which would have benefited the expansion in ranges of various faunas, including *H. sapiens* (56). Such optimum environmental conditions, together with the greater climatic tolerance of *H. sapiens* that developed during ~300–100 ka (4, 7), plausibly provided an unprecedented opportunity for AMH dispersal to East Asia during the last interglacial. According to the habitat map averaged over 125–70 ka (Fig. 4C), transcontinental optimal habitats might have stimulated AMH populations to disperse from their African homeland to East Asia via southern (South Asia) and northern routes (continental Central Asia). An earlier (pre-70-ka) AMH dispersal utilizing the southern route to East Asia is most consistent with ASM strengthening (Fig. 3). Moreover, the southern dispersal route lies under strong, continual ASM influence and is supported by the MIS 5 AMH archeological evidence from India, including the sites of Sandhav (~110 ka) (57), Katoati (96 ka) (58), Jwalapuram (85–75 ka) (59), and Sri Lanka (74–64 ka) (58) (Figs. 1 and 4C). Although recent findings suggest that early *H. sapiens* may have dispersed to Greece (Europe) and Israel (West Asia) as early as ~200 ka (60, 61), *H. sapiens* fossil/archeological evidence remains currently absent from MIS 6–5 Central Asia (8). This absence probably indicates that the relatively colder/drier northern dispersal route beyond the ASM reach may have occurred later than the southern route (8, 62), with an initial failure in competition with pre-existing populations of Denisovans or Neanderthals (36, 63) (Fig. 4C).

Before the *H. sapiens* appearance, East Asia was occupied by a number of hominins characterized by a mosaic of plesiomorphic features with derived traits (such as enlarged cranial capacity, facial gracilization, simplified enamel-dentine junction surfaces or symmetrical premolar crowns). These samples include fossils recovered from either Huanglong Cave, Harbin, Panxian Dadong, Xuchang, Dali or Tongzi (43, 64-70). They have been tentatively classified as “non-erectus” Asian Mid-Pleistocene

hominins (65, 70). However, we find that the large majority of East Asian *H. sapiens* and other hominin sites older than 70 ka are consistently under ASM influence. Lower latitudes with higher ASM precipitation contain more hominin sites of the late Mid-Pleistocene and early Late Pleistocene than higher latitudes with lower ASM precipitation. Particularly, almost all robustly dated pre-70-ka *H. sapiens* evidence is found from Southeast Asia with wetter and greener landscapes under continual ASM influence. These observations are consistent with a close link between hominin occupation and the ASM. The ASM-induced changes in the habitats of East Asian hominins affected their mobility and possibly their degrees of isolation, which in turn may have affected the probability of their mixing and interbreeding (71). Although we are far from understanding the phenotypic signal of interbreeding (72), we cannot rule out that part of the anatomical variability of the late-Middle to Late Pleistocene groups in Asia is related to the admixture of *H. sapiens* with the pre-existing indigenous populations at the time of AMH's arrival (73).

In contrast to a shift to wetter conditions in East Asia induced by ASM strengthening as suggested by our both proxy- and model-based hydroclimatic reconstructions (Fig. 2), large areas of Southeast Africa—the major homeland of *H. sapiens*—had a deteriorating climate during MIS 6–5 transition (3, 74-78). For example, paleoclimatic records from the Limpopo catchment, KwaZulu-Natal, and Lake Magadi suggests a series of "megadroughts" in subtropical Southeast Africa during MIS 5 (74-76). A principal component analysis of hydrologically sensitive fossil and mineralogical records from the Lake Malawi suggests that tropical Southeast Africa was largely drier during MIS 5 relative to MIS 6 (78). The deterioration of climatic conditions could have decreased vegetation and reduced mammal populations and the availability of resources and habitats. This is confirmed by our *H. sapiens* habitat simulation, which suggests that habitat peaks and troughs in East Africa and habitat peaks in South

Africa lowered during MIS 5, in comparison to the preceding MIS 6 (Fig. S10). This in turn enhanced selective pressures, so *H. sapiens* may have been forced to expand beyond Africa and into the nearby West Asia. Upon arrival of *H. sapiens* populations in the West Asian regions around the Mediterranean Sea, as indicated by evidence from Israel (79-81), some may have dispersed further to remote East Asia during MIS 5, when increased ASM precipitation produced suitable conditions with abundant resources (e.g., food, water, and shelter), attracting *H. sapiens* colonization. The combination of climate deterioration in large areas of Southeast African and favorable climate in East Asia may have promoted continental-scale early *H. sapiens* dispersal to East Asia during MIS 5.

To summarize, through synthesis of new proxy- and model-based East Asian climate reconstructions, compilations of Asian paleoanthropological and paleoclimatic data, and *H. sapiens* habitat simulations through time and space, we improve current understanding of orbital-scale ASM dynamics, and more importantly, reveal the close links between ASM climate and initial AMH dispersal to East Asia. New centennial-resolution environmental magnetic records derived from a unique high sedimentation rate loess-paleosol section on the central CLP, together with the latest proxy records from other parts of the plateau (12, 20, 22), document a pervasive precession signal in the hydroclimatic evolution across the CLP, in addition to the well-recognized ~100-kyr cyclicity. Our results provide new Asian evidence for previously suggested complex models explaining the origin and dispersal(s) of *H. sapiens*, which points to less linear evolutionary scenarios where climatic changes likely played a major role in the dispersals, fragmentation, assimilation and recombination of new immigrant populations with pre-existing local groups (71, 82, 83). Integration of paleoclimate data with compiled hominin fossil and archeological finds from Asia and simulated *H. sapiens* habitats shows that increased monsoonal rain and higher temperature across the Asian continent, together with climate deterioration in Southeast

298 Africa, provided an optimum window of opportunity for early AMH dispersals to remote East Asia
299 during the last interglacial.

300

301 ## Methods

302 Following removal of weathered surface outcrop, 2,066 fresh samples were collected from paleosol $S_0$
303 (MIS 1) to loess $L_3$ (MIS 8) at 2–2.5 cm intervals (equivalent to ~0.1–0.8 kyr time spacing) from the
304 Huanxian loess-paleosol section. About 10 g of each sample was powdered and then packed into a
305 nonmagnetic cubic box (2 cm × 2 cm × 2 cm) for χ and ARM measurements in the laboratory. We
306 measured room temperature χ using a SM-150L magnetic susceptibility meter (ZH instruments, Czech
307 Republic) at a frequency of 500 Hz and an applied field of 80 A/m at the Institute of Earth Environment,
308 Chinese Academy of Sciences, Xi'an, China. ARM was imparted using a peak alternating field (AF) of
309 100 mT and a 0.05 mT direct current (DC) bias field and was measured using a 2-G Enterprises Model
310 755 cryogenic magnetometer housed in a magnetically shielded space at the China University of
311 Geosciences (Wuhan), China.

312 We stablished a first-order chronology for the Huxian loess-paleosol section based on the well
313 identified cycle-based correlation between CLP loess-paleosol χ and marine benthic foraminiferal $\delta^{18}O$
314 records (24, 25) (Fig. S2A–B). In addition to the top and bottom points, six extra points around the
315 transitions between high and low χ units were used as tie points to construct this first-order chronology
316 (Fig. S2B). Both CLP χ and East China speleothem $\delta^{18}O$ records are grossly linked to the same
317 large-scale shifts in ASM circulation (15, 24, 25, 84). We further refined the first-order chronology by
318 repeatedly matching χ with the precisely-dated composite East China speleothem $\delta^{18}O$ record (15) in an

objective way until their cycles are synchronized to in-phase variations (Fig. S2C). This recently developed approach enables a more precise speleothem-based CLP loess-paleosol chronology relative to previous age models based on land-sea correlation or orbital tuning (12, 28, 85). In addition to the eight points selected for the first-order chronology construction, we selected seven additional tie points either located on high-amplitude χ peaks of the well-developed strong pedogenic interglacial paleosol $S_2$ or at the onset/termination of relatively weaker pedogenic sub-paleosols (corresponding to somewhat moister interstadials and lower-amplitude χ peaks) within glacial loess layers, to construct the refined age model for the Huanxian loess-paleosol section based on cyclic correlation between the χ and East China speleothem $\delta^{18}O$ records (Fig. S2C). This refined chronology is supported independently by recent optically stimulated luminescence dating of the Jingbian loess-paleosol section on the northern CLP margin (29) (Fig. S2D). The Huanxian χ data on the refined chronology closely follow the speleothem $\delta^{18}O$ record over precessional cycles (Fig. S2C). Land-sea correlation and loess-speleothem match, with distinct tie point selection, do not result in significant differences in the CLP loess-paleosol age models, generally with only millennial differences (22, 24-26, 28).

We established a new ASM stack by compiling proxy records from East Asia, including the Huanxian χ and ARM records, the Jingyuan carbonate $\delta^{13}C$ record (22), the Xijing spliced grain size-χ stack (20), and the Baoji $^{10}Be$-based precipitation reconstruction (12). Like our established Huanxian χ and ARM time series above, we first refined age models for the Jingyuan carbonate $\delta^{13}C$ record (22), Xijing spliced grain size-χ stack (20), and Baoji $^{10}Be$-based precipitation record (12) by synchronizing them to the precisely U/Th-dated East China speleothem $\delta^{18}O$ record (15). After synchronization, we used the interpolating function in the *Acycle* software (86) to conservatively resample all used records at 0.5-kyr intervals to obtain evenly spaced data series. We constructed the ASM stack from the CLP by

averaging the evenly-spaced Huanxian χ and ARM, Jingyuan carbonate $\delta^{13}C$, Xijing spliced grain size-χ stack, and Baoji $^{10}Be$-based precipitation time series with equal weight. To evaluate the robustness of the orbital signature, we used the smoothed periodogram to analyze the power spectra of proxy- and model-based paleoclimatic reconstructions with the function Spectral Analysis in the *Acycle* software (86), with a bandwidth of 2 and a sampling interval of 1 kyr.

To identify the magnetic minerals in the sediments, we measured temperature-dependent magnetic susceptibility curves (χ–T), isothermal remanent magnetization (IRM) acquisition curves, magnetic hysteresis loops, first-order reversal curve (FORC) diagrams, and low temperature cycles of the saturation isothermal remanent magnetization (SIRM) for nine samples from the Huanxian section at the Institute of Earth Environment, Chinese Academy of Sciences, Xi'an, China. They contain four loess samples from loess layers $L_1$, $L_2$, and $L_3$, and five paleosol samples from paleosol layers $S_0$, $S_1$, and $S_2$. χ–T curves were measured in an argon atmosphere from room temperature to 700 °C and back to room temperature with a MFK1-FA susceptometer equipped with a CS-3 high-temperature furnace (AGICO, Brno, Czech Republic). IRM acquisition curves, magnetic hysteresis loops, and FORC diagrams were measured with a Princeton Measurements Corporation (Model 3900) vibrating sample magnetometer (VSM). Each IRM acquisition curve contains 200 data points measured at logarithmically spaced field steps to 1 T. Each hysteresis loop was measured between ±1 T at 3 mT increments, with a 300 ms averaging time. For each sample, 80 FORCs were measured at 5 mT increments to ~600 mT, with a 100 ms averaging time. Low-temperature magnetic measurements were conducted with a Quantum Design superconducting quantum interference device (SQUID) Magnetic Property Measurement System (MPMS) (Quantum Design Inc, USA). A room temperature saturation isothermal remanent

magnetization (SIRM), which was imparted in a 5 T field at 300 K, was measured at 5 K intervals from 300 to 5 K and back to 300 K in zero magnetic field.

**Data availability.** All of our measured proxy data are included in the Dataset and will be available in the East Asian Paleoenvironmental Science Database.

**ACKNOWLEDGMENTS.** We thank five anonymous reviewers for their constructive comments. This study was supported financially by the Chinese Academy of Sciences (CAS) Strategic Priority Research Program (XDB 40000000), the Second Tibetan Plateau Scientific Expedition and Research (STEP) program (2019QZKK0707), the National Natural Science Foundation of China, the Shaanxi Provence Youth Talent Support Program, the Chinese Academy of Sciences Key Research Program of Frontier Sciences (QYZDB-SSW-DQC021), and the State Key Laboratory of Loess and Quaternary Geology, Institute of Earth Environment, Chinese Academy of Sciences. M.M.-T. receives funding from Project PID2021-122355NB-C33 financed by MCIN/ AEI/10.13039/501100011033/ FEDER, UE and The Leakey Foundation through the personal support of Dub Crook.

**Author Contributions:** H.A. designed this research. J.R. analyzed the habitat simulation of *H. sapiens*. M.M.-T. contributed to the paleoanthropological interpretation. M.K. calculated the model-based East Asian climate reconstructions. J.L.J. and Z.Y.Z. carried out the laboratory analysis. X.X.L. undertook the spectral analysis. J.R., D.L., M.J.D., T.C., T.N.J., Z.M.Z., C.J.H, Q.S., P.G.Y., X.Z.L., X.X.X., Y.G.S.,

X.K.Q., P.Z., and Z.S.A. contributed to paleoclimatic data analysis, interpretation and discussion. H.A. wrote the manuscript with contributions from all other authors.

## References


1. J. J. Hublin *et al.*, New fossils from Jebel Irhoud, Morocco and the pan-African origin of *Homo sapiens*. *Nature* **546**, 289–292 (2017).
2. C. M. Vidal *et al.*, Age of the oldest known *Homo sapiens* from eastern Africa. *Nature* **601**, 579–583 (2022).
3. J. E. Tierney, P. B. deMenocal, P. D. Zander, A climatic context for the out-of-Africa migration. *Geology* **45**, 1023–1026 (2017).
4. R. M. Beyer, M. Krapp, A. Eriksson, A. Manica, Climatic windows for human migration out of Africa in the past 300,000 years. *Nat. Commun.* **12**, 4889, doi: 10.1038/s41467-021-24779-1 (2021).
5. F. Schaebitz *et al.*, Hydroclimate changes in eastern Africa over the past 200,000 years may have influenced early human dispersal. *Commun. Earth Environ.* **2**, 123, doi: 10.1038/s43247-021-00195-7 (2021).
6. A. Timmermann, T. Friedrich, Late Pleistocene climate drivers of early human migration. *Nature* **538**, 92–95 (2016).
7. A. Timmermann *et al.*, Climate effects on archaic human habitats and species successions. *Nature* **604**, 495–501 (2022).
8. C. J. Bae, K. Douka, M. D. Petraglia, On the origin of modern humans: Asian perspectives.

*Science* **358**, eaai9067 (2017).

9. R. Dennell, *From Arabia to the Pacific: How our species colonised Asia* (Routledge, London, 2020), pp. 386.

10. C. J. Bae, F. Li, L. L. Cheng, W. Wang, H. L. Hong, Hominin distribution and density patterns in Pleistocene China: Climatic influences. *Palaeogeogr. Palaeoclimatol. Palaeoecol.* **512**, 118–131 (2018).

11. S. C. Clemens *et al.*, Precession-band variance missing from East Asian monsoon runoff. *Nat. Commun.* **9**, 3364, doi: 10.1038/s41467-018-05814-0 (2018).

12. J. W. Beck *et al.*, A 550,000-year record of East Asian monsoon rainfall from $^{10}$Be in loess. *Science* **360**, 877–881 (2018).

13. Y. J. Cai *et al.*, Variability of stalagmite-inferred Indian monsoon precipitation over the past 252,000 y. *Proc. Natl. Acad. Sci. U.S.A.* **112**, 2954–2959 (2015).

14. T. Caley *et al.*, New Arabian Sea records help decipher orbital timing of Indo-Asian monsoon. *Earth Planet. Sci. Lett.* **308**, 433–444 (2011).

15. H. Cheng *et al.*, The Asian monsoon over the past 640,000 years and ice age terminations. *Nature* **534**, 640–646 (2016).

16. H. Cheng *et al.*, Milankovitch theory and monsoon. *The Innovation* **3**, 100338, doi: 10.1016/j.xinn.2022.100338 (2022).

17. S. C. Clemens *et al.*, Remote and local drivers of Pleistocene South Asian summer monsoon precipitation: A test for future predictions. *Sci. Adv.* **7**, eabg3848 (2021).

18. S. M. McGrath, S. C. Clemens, Y. S. Huang, M. Yamamoto, Greenhouse gas and ice volume drive Pleistocene Indian summer monsoon precipitation isotope variability. *Geophys. Res. Lett.*

**48**, e2020GL092249, doi: 10.1029/2020GL092249 (2021).

19. D. Gebregiorgis *et al.*, Southern Hemisphere forcing of South Asian monsoon precipitation over the past ~1 million years. *Nat. Commun.* **9**, 4702, doi: 10.1038/s41467-018-07076-2 (2018).

20. B. H. Guo *et al.*, Dominant precessional forcing of the East Asian summer monsoon since 260 ka. *Geology* **50**, 1372–1376 (2022).

21. Y. B. Sun *et al.*, Astronomical and glacial forcing of East Asian summer monsoon variability. *Quat. Sci. Rev.* **115**, 132–142 (2015).

22. Y. B. Sun *et al.*, Diverse manifestations of the mid-Pleistocene climate transition. *Nat. Commun.* **10**, 352 doi: 10.1038/s41467-41018-08257-41469 (2019).

23. M. Krapp, R. M. Beyer, S. L. Edmundson, P. J. Valdes, A. Manica, A statistics-based reconstruction of high-resolution global terrestrial climate for the last 800,000 years. *Sci. Data* **8**, 228, doi: 10.1038/s41597-021-01009-3 (2021).

24. H. Ao *et al.*, Two-stage mid-Brunhes climate transition and mid-Pleistocene human diversification. *Earth-Sci Rev* **210**, 103354 (2020).

25. Q. Z. Hao *et al.*, Delayed build-up of Arctic ice sheets during 400,000-year minima in insolation variability. *Nature* **490**, 393–396 (2012).

26. Z. L. Ding *et al.*, Stacked 2.6-Ma grain size record from the Chinese loess based on five sections and correlation with the deep-sea $\delta^{18}O$ record. *Paleoceanography* **17**, 1033, doi:1010.1029/2001PA000725 (2002).

27. Y. B. Sun, S. C. Clemens, Z. S. An, Z. W. Yu, Astronomical timescale and palaeoclimatic implication of stacked 3.6-Myr monsoon records from the Chinese Loess Plateau. *Quat. Sci. Rev.* **25**, 33–48 (2006).

28. Y. B. Sun *et al.*, High-sedimentation-rate loess records: A new window into understanding orbital- and millennial-scale monsoon variability. *Earth-Sci Rev* **220**, 103731 (2021).

29. T. Stevens *et al.*, Ice-volume-forced erosion of the Chinese Loess Plateau global Quaternary stratotype site. *Nat. Commun.* **9**, 983, doi: 910.1038/s41467-41018-03329-41462 (2018).

30. E. J. Rohling *et al.*, Sea level and deep-sea temperature reconstructions suggest quasi-stable states and critical transitions over the past 40 million years. *Sci. Adv.* **7**, eabf5326 (2021).

31. B. Bereiter *et al.*, Revision of the EPICA Dome C $CO_2$ record from 800 to 600 kyr before present. *Geophys. Res. Lett.* **42**, 542–549 (2015).

32. J. Laskar, A. Fienga, M. Gastineau, H. Manche, La2010: A new orbital solution for the long term motion of the Earth. *Astron. Astrophys.* **532**, A89 (2011).

33. Z. K. Zhang, G. J. Li, Y. J. Cai, Z. Y. Liu, Z. S. An, Variation of summer precipitation $\delta^{18}O$ on the Chinese Loess Plateau since the last interglacial. *J. Quat. Sci.* **36**, 1214–1220 (2021).

34. C. J. Bae *et al.*, Modern human teeth from Late Pleistocene Luna Cave (Guangxi, China). *Quat. Int.* **354**, 169–183 (2014).

35. W. Liu *et al.*, Human remains from Zhirendong, South China, and modern human emergence in East Asia. *Proc. Natl. Acad. Sci. U.S.A.* **107**, 19201–19206 (2010).

36. W. Liu *et al.*, The earliest unequivocally modern humans in southern China. *Nature* **526**, 696–699 (2015).

37. X. F. Sun *et al.*, Ancient DNA and multimethod dating confirm the late arrival of anatomically modern humans in southern China. *Proc. Natl. Acad. Sci. U.S.A.* **118**, e2019158118 (2021).

38. M. Martinón-Torres *et al.*, On the misidentification and unreliable context of the new “human teeth” from Fuyan Cave (China). *Proc. Natl. Acad. Sci. U.S.A.* **118**, e2102961118 (2021).

469 39. T. F. G. Higham, K. Douka, The reliability of late radiocarbon dates from the Paleolithic of
470 southern China. *Proc. Natl. Acad. Sci. U.S.A.* **118**, e2103798118 (2021).
471 40. G. J. Shen *et al.*, U-Series dating of Liujiang hominid site in Guangxi, Southern China. *J. Hum.*
472 *Evol.* **43**, 817–829 (2002).
473 41. G. J. Shen, W. Wang, Q. Wang, Y. J. Pan, U-series dating of hominid site Ganqian Cave at Tubo,
474 Liujiang, Guangxi in South China. *Acta Anthropol. Sin.* **20**, 238–244 (2001).
475 42. W. Wang, C. L. Huang, S. W. Xie, C. L. Yan, Late Pleistocene hominin teeth from the Jimuyan
476 Cave, Pingle County, Guangxi, South China. *Quat. Sci.* **31**, 699–704 (2011).
477 43. W. Liu, X. J. Wu, S. Xing, Y. Y. Zhang, *Human Fossils in China* (Science Press, Beijing, 2014),
478 pp. 388.
479 44. H. Shang, W. Liu, X. Z. Wu, G. R. Dong, Upper Pleistocene human scapula from Salawusu,
480 Inner Mongolia, China. *Chin. Sci. Bull.* **51**, 2110–2115 (2006).
481 45. H. Shang, Q. Wei, X. H. Wu, An issue on the date of fossil human remains from Sala wusu, Inner
482 Mongolia. *Acta Anthropol. Sin.* **25**, 82–86 (2006).
483 46. M. Martinón-Torres, X. J. Wu, J. M. Bermúdez de Castro, S. Xing, W. Liu, *Homo sapiens* in the
484 Eastern Asian Late Pleistocene. *Curr. Anthropol.* **58**, S434–S448 (2017).
485 47. C. Bae, P. Guyomarc'h, Potential contributions of Korean Pleistocene hominin fossils to
486 palaeoanthropology: A view from Ryonggok Cave. *Asian Perspect.* **54**, 31–57 (2015).
487 48. C. J. Norton, The current state of Korean paleoanthropology. *J. Hum. Evol.* **38**, 803–825 (2000).
488 49. K. E. Westaway *et al.*, An early modern human presence in Sumatra 73,000–63,000 years ago.
489 *Nature* **548**, 322–325 (2017).
490 50. S. E. Freidline *et al.*, Early presence of *Homo sapiens* in southeast Asia by 86–68 kyr at Tam Pà

Ling, northern Laos. *Nat. Commun.* **14**, 3193, doi: 10.1038/s41467-023-38715-y (2023).

51. C. Clarkson *et al.*, Human occupation of northern Australia by 65,000 years ago. *Nature* **547**, 306–310 (2017).

52. L. Pagani *et al.*, Genomic analyses inform on migration events during the peopling of Eurasia. *Nature* **538**, 238–242 (2016).

53. M. Kuhlwilm *et al.*, Ancient gene flow from early modern humans into eastern Neanderthals. *Nature* **530**, 429–433 (2016).

54. R. Dennell, Early *Homo sapiens* in China. *Nature* **468**, 512–513 (2010)..

55. R. Dennell, M. D. Petraglia, The dispersal of *Homo sapiens* across southern Asia: How early, how often, how complex? *Quat. Sci. Rev.* **47**, 15–22 (2012).

56. I. A. Lazagabaster *et al.*, Rare crested rat subfossils unveil Afro–Eurasian ecological corridors synchronous with early human dispersals. *Proc. Natl. Acad. Sci. U.S.A.* **118**, e2105719118 (2021).

57. J. Blinkhorn *et al.*, The first directly dated evidence for Palaeolithic occupation on the Indian coast at Sandhav, Kachchh. *Quat. Sci. Rev.* **224**, 105975, doi: 10.1016/j.quascirev.2019.105975 (2019).

58. J. Blinkhorn, M. D. Petraglia, Environments and cultural change in the Indian subcontinent: Implications for the dispersal of *Homo sapiens* in the Late Pleistocene. *Curr. Anthropol.* **58**, 463–479 (2017).

59. M. Petraglia *et al.*, Middle Paleolithic assemblages from the Indian subcontinent before and after the Toba super-eruption. *Science* **317**, 114–116 (2007).

60. K. Harvati *et al.*, Apidima Cave fossils provide earliest evidence of *Homo sapiens* in Eurasia.

*Nature* **571**, 500–504 (2019).

61. I. Hershkovitz *et al.*, The earliest modern humans outside Africa. *Science* **359**, 456–459 (2018).

62. T. Goebel, "The overland dispersal of modern humans to eastern Asia: An alternative, northern route from Africa" in Emergence and diversity of modern human behavior in Paleolithic, Y. Kaifu, T. Goebel, H. Sato, A. Ono, Eds. ( Texas A&M University Press, College Station,2015), pp. 437–452.

63. N. Zwyns *et al.*, The northern route for human dispersal in central and northeast Asia: New evidence from the site of Tolbor-16, Mongolia. *Sci. Rep.* **9**, 1–10 (2019).

64. X. J. Ni *et al.*, Massive cranium from Harbin in northeastern China establishes a new Middle Pleistocene human lineage. *The Innovation* **2**, 100130, doi: 10.1016/j.xinn.2021.100130 (2021).

65. S. Xing, M. Martinón-Torres, J. M. Bermúdez de Castro, Late Middle Pleistocene hominin teeth from Tongzi, southern China. *J. Hum. Evol.* **130**, 96–108 (2019).

66. W. Liu *et al.*, Late Middle Pleistocene hominin teeth from Panxian Dadong, South China. *J. Hum. Evol.* **64**, 337–355 (2013).

67. Z. Y. Li *et al.*, Late Pleistocene archaic human crania from Xuchang, China. *Science* **355**, 969–972 (2017).

68. X. Z. Wu, S. Athreya, A description of the geological context, discrete traits, and linear morphometrics of the Middle Pleistocene hominin from Dali, Shaanxi Province, China. *Am. J. Phys. Anthropol.* **150**, 141–157 (2013).

69. X. J. Wu *et al.*, Archaic human remains from Hualongdong, China, and Middle Pleistocene human continuity and variation. *Proc. Natl. Acad. Sci. U.S.A.* **116**, 9820–9824 (2019).

70. X. J. Wu *et al.*, Morphological and morphometric analyses of a late Middle Pleistocene hominin

mandible from Hualongdong, China. *J. Hum. Evol.* **182**, 103411, doi: 10.1016/j.jhevol.2023.103411 (2023).

71. R. Dennell, M. Martinón-Torres, J.-M. Bermúdez de Castro, G. Xing, A demographic history of Late Pleistocene China. *Quat. Int.* **559**, 4–13 (2020).

72. R. R. Ackermann, Phenotypic traits of primate hybrids: Recognizing admixture in the fossil record. *Evol. Anthropol.* **19**, 258–270 (2010).

73. W. Liao *et al.*, Mosaic dental morphology in a terminal Pleistocene hominin from Dushan Cave in southern China. *Sci. Rep.* **9**, 2347, doi: 10.1038/s41598-019-38818-x (2019).

74. T. Caley *et al.*, A two-million-year-long hydroclimatic context for hominin evolution in southeastern Africa. *Nature* **560**, 76–79 (2018).

75. M. H. Simon *et al.*, Eastern South African hydroclimate over the past 270,000 years. *Sci. Rep.* **5**, 18153, doi: 10.1038/srep18153 (2015).

76. R. B. Owen *et al.*, Progressive aridification in East Africa over the last half million years and implications for human evolution. *Proc. Natl. Acad. Sci. U.S.A.* **115**, 11174–11179 (2018).

77. T. C. Johnson *et al.*, A progressively wetter climate in southern East Africa over the past 1.3 million years. *Nature* **537**, 220–224 (2016).

78. S. J. Ivory *et al.*, Environmental change explains cichlid adaptive radiation at Lake Malawi over the past 1.2 million years. *Proc. Natl. Acad. Sci. U.S.A.* **113**, 11895–11900 (2016).

79. R. Grün *et al.*, U-series and ESR analyses of bones and teeth relating to the human burials from Skhul. *J. Hum. Evol.* **49**, 316–334 (2005).

80. D. E. Bar-Yosef Mayer, B. Vandermeersch, O. Bar-Yosef, Shells and ochre in Middle Paleolithic Qafzeh Cave, Israel: Indications for modern behavior. *J. Hum. Evol.* **56**, 307–314 (2009).

81. H. P. Schwarcz *et al.*, ESR dates for the hominid burial site of Qafzeh in Israel. *J. Hum. Evol.* **17**, 733–737 (1988).

82. C. Stringer, The origin and evolution of *Homo sapiens*. *Philos. T. R. Soc. B.* **371**, 20150237, doi: 10.1098/rstb.2015.0237 (2016).

83. M. Martinón-Torres, S. Xing, W. Liu, J.-M. Bermúdez de Castro, A "source and sink" model for East Asia? Preliminary approach through the dental evidence. *C. R. Palevol* **17**, 33–43 (2018).

84. Y. J. Wang *et al.*, Millennial- and orbital-scale changes in the East Asian monsoon over the past 224,000 years. *Nature* **451**, 1090–1093 (2008).

85. Y. B. Sun *et al.*, Persistent orbital influence on millennial climate variability through the Pleistocene. *Nat. Geosci.* **14**, 812–818 (2021).

86. M. S. Li, L. Hinnov, L. Kump, Acycle: Time-series analysis software for paleoclimate research and education. *Comput. Geosci.* **127**, 12–22 (2019).

570 Figure captions:

571 **Figure 1. Study context.** African and Eurasian annual precipitation map averaged between 130 and 70
572 ka from the latest model-based climate reconstructions (23), with referenced paleoclimatic and
573 archaeological sites in Asia, Tibetan Plateau (>2000 m topography), and schematized African and Asian
574 monsoon circulations. Background data for the listed Asian *H. sapiens* sites are included in Table S1.

575 **Figure 2. Proxy- and model-based reconstructions of orbital-scale East Asian climate variability.**
576 (**A**) Lithology, (**B**) magnetic susceptibility ($\chi$, green curve), and (**C**) ARM (brown curve) from the
577 Huanxian loess-paleosol section with their comparison with 30°N July insolation (32) (red curve) and
578 their power spectra. S-numbers and L-numbers refer to consecutive paleosol and loess horizons counting
579 back from the present-day, respectively. Time series and power spectra of (**D**) sea level reconstruction
580 from a global benthic foraminiferal $\delta^{18}O$ stack (30) and (**E**) atmospheric $CO_2$ reconstruction from
581 Antarctic ice core (31). Numbers on the sea level record refer to the successive marine isotope stages.
582 Time series and power spectra of (**F**) annual and (**G**) summer precipitation over North China (100–
583 120°E; 30–45°N), (**H**) annual and (**I**) summer precipitation over South China (100–120°E; 20–30°N), (**J**)
584 average summer surface temperature over low-latitude East Asia (100–120°E, 20°N), (**K**) summer
585 precipitable moisture on the West Pacific and North Indian oceans (80–150°E; 0–35°N), (**L**) summer
586 wind speed, in response to combined ice volume, atmospheric $CO_2$ concentration, and insolation forcing,
587 which are calculated from the latest model-based climate reconstructions (23). Summer is represented by
588 May to September. (**M**) International Ocean Discovery Program (IODP) Site U1429 Mg/Ca sea surface
589 temperature (SST) record from the East China Sea (11) and its power spectrum. The dashed lines in the
590 power spectra (right panel) denote regions statistically significantly above the 95% confidence level

591 (Student's *t*-test). The vertical shading indicates the approximate timing of early AMH arrivals in East
592 Asia.

593 **Figure 3. Climatic context for early *H. sapiens* dispersal to East Asia.** Time series and power spectra
594 of (**A**) new CLP ASM stack based on the Huanxian χ and ARM records, the Jingyuan carbonate $\delta^{13}C$
595 record (22), the Xijing spliced grain size-χ stack (20), and the Baoji $^{10}Be$-based precipitation record (12),
596 (**B**) China composite speleothem $\delta^{18}O$ record (15), (**C**) speleothem $\delta^{18}O$ from Xiaobailong Cave, South
597 China (13), (**D, E**) Indian margin Site U1446 sediment core seawater $\delta^{18}O$ and $\delta D_{wax}$ records (17, 18),
598 and (**F**) summer monsoon stack from sediment core MD04-2861, Arabian Sea (14). The vertical shading
599 indicates the approximate timing of early AMH arrivals in East Asia.

600 **Figure 4. *Homo sapiens* habitat suitability.** (**A**) Raw and aggregated age distributions of early *H.*
601 *sapiens* fossils from China, including Luna Cave (120–70 ka) (34), Zhiren Cave (113–100 ka) (35),
602 Tongtianyan Cave (Liujiang, 130–70 ka) (40), Ganqian Cave (140–100 ka) (41), and Fuyan Cave (120–
603 80 ka) (36), and from Southeast Asia represented by Tam Pà Ling (86–68 ka) in Northern Laos (50) and
604 Lida Ajer Cave (73–63 ka) in Sumatra (49). (**B**) Simulated timeseries of *H. sapiens* habitat suitability in
605 East Asia during the last 280 kyr and (**C**) simulated *H. sapiens* habitat map over 125–70 ka (7) with
606 occupied localities by *H. neanderthalensis*, Denisovans and early *H. sapiens*.

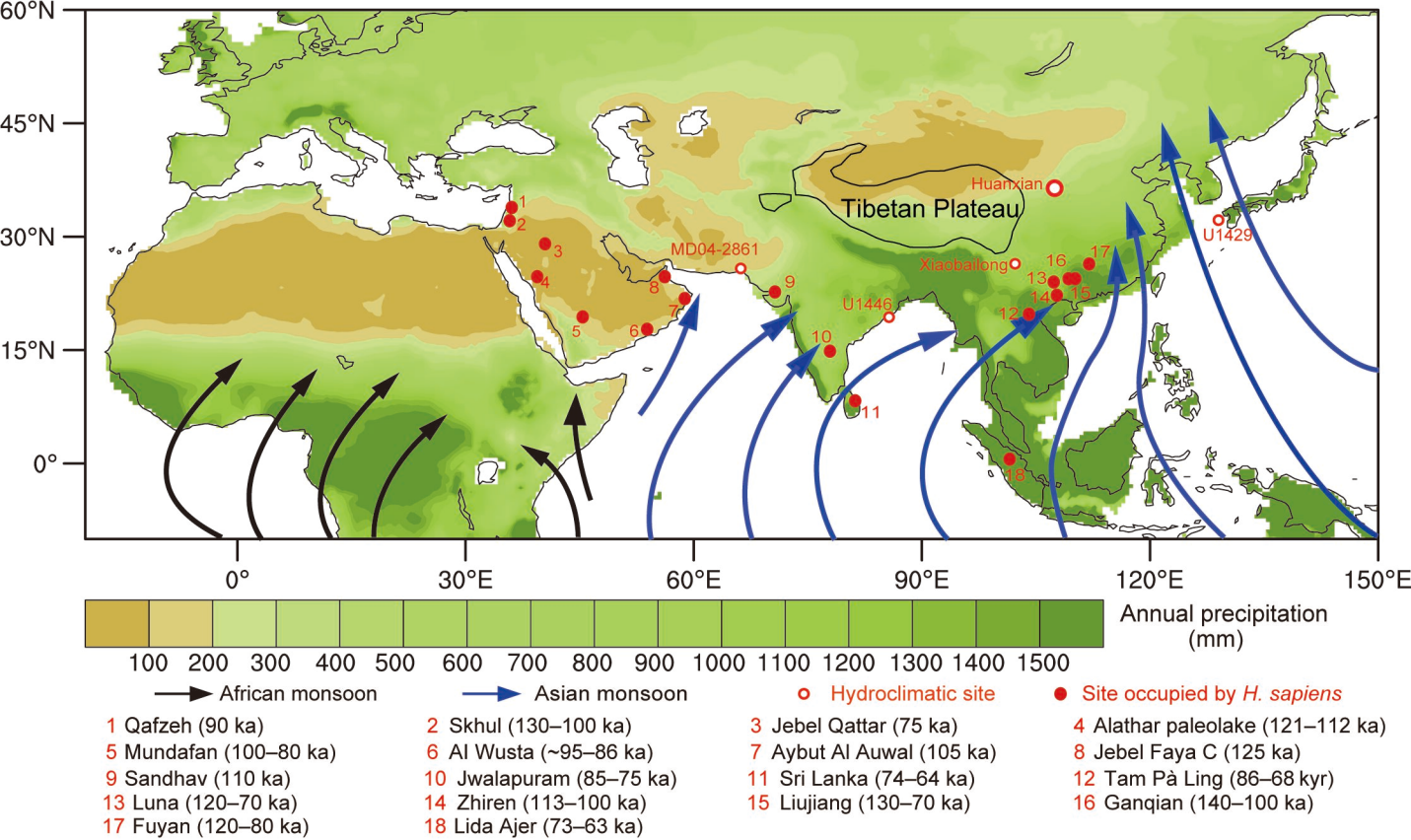
60°N
45°N
30°N
15°N
0°
0°
30°E
60°E
90°E
120°E
150°E
Tibetan Plateau
Huanxian
U1429
MD04-2861
Xiaobailong
U1446
1
2
3
4
5
6
7
8
9
10
11
12
13
14
15
16
17
18
Annual precipitation (mm)
100 200 300 400 500 600 700 800 900 1000 1100 1200 1300 1400 1500
African monsoon
Asian monsoon
Hydroclimatic site
Site occupied by H. sapiens
1 Qafzeh (90 ka)
2 Skhul (130–100 ka)
3 Jebel Qattar (75 ka)
4 Alathar paleolake (121–112 ka)
5 Mundafan (100–80 ka)
6 Al Wusta (~95–86 ka)
7 Aybut Al Auwal (105 ka)
8 Jebel Faya C (125 ka)
9 Sandhav (110 ka)
10 Jwalapuram (85–75 ka)
11 Sri Lanka (74–64 ka)
12 Tam Pà Ling (86–68 kyr)
13 Luna (120–70 ka)
14 Zhiren (113–100 ka)
15 Liujiang (130–70 ka)
16 Ganqian (140–100 ka)
17 Fuyan (120–80 ka)
18 Lida Ajer (73–63 ka)

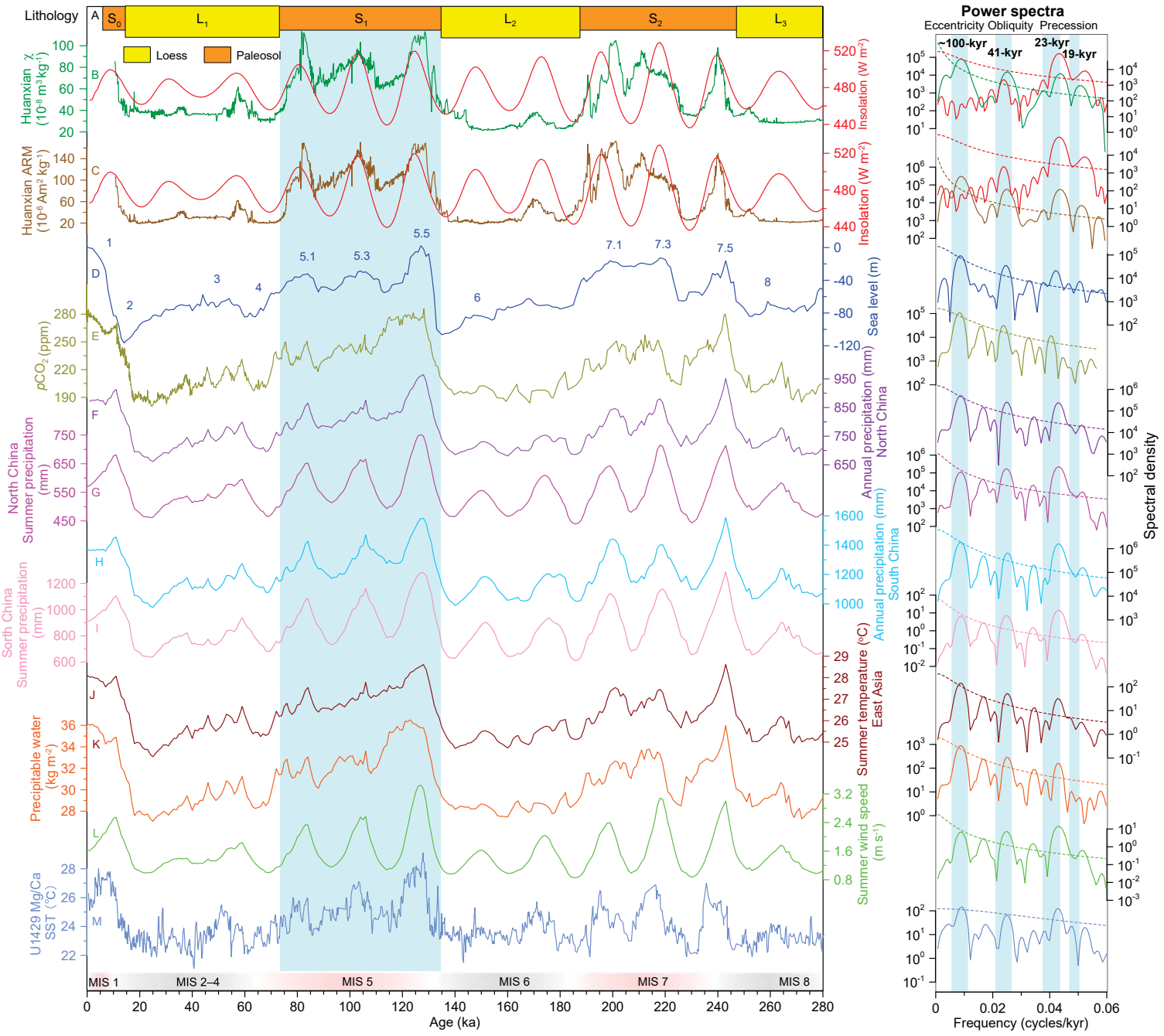
Lithology
A
S0
L1
S1
L2
S2
L3
Loess
Paleosol
Huanxian χ (10-8 m3 kg-1)
B
Huanxian ARM (10-6 Am2 kg-1)
C
Insolation (W m-2)
D
Sea level (m)
pCO2 (ppm)
E
North China Summer precipitation (mm)
F
G
Annual precipitation (mm) North China
Sorth China Summer precipitation (mm)
H
I
Annual precipitation (mm) South China
Precipitable water (kg m-2)
J
K
Summer temperature (°C) East Asia
L
Summer wind speed (m s-1)
U1429 Mg/Ca SST (°C)
M
MIS 1
MIS 2–4
MIS 5
MIS 6
MIS 7
MIS 8
Age (ka)
Power spectra
Eccentricity Obliquity Precession
100-kyr
41-kyr
23-kyr
19-kyr
Spectral density
Frequency (cycles/kyr)

East Asian monsoon

CLP ASM stack

A

(This study)

B

(Cheng et al., 2016)

Speleothem $\delta^{18}O$ (‰) East China

Xiaobailong Cave Speleothem $\delta^{18}O$ (‰)

C

(Cai et al., 2015)

(Clemens et al., 2021)

D

Seawater $\delta^{18}O$ (‰) U1446

South Asian (Indian) monsoon

U1446 Leaf wax $\delta D$ (‰)

(McGrath et al., 2021)

E

F

(Caley et al., 2011)

Summer monsoon stack MD04-2861

MIS 1 MIS 2–4 MIS 5 MIS 6 MIS 7 MIS 8

Age (ka)

Power spectra

~100-kyr 41-kyr 23-kyr 19-kyr

Spectral density

Frequency (cycles/kyr)

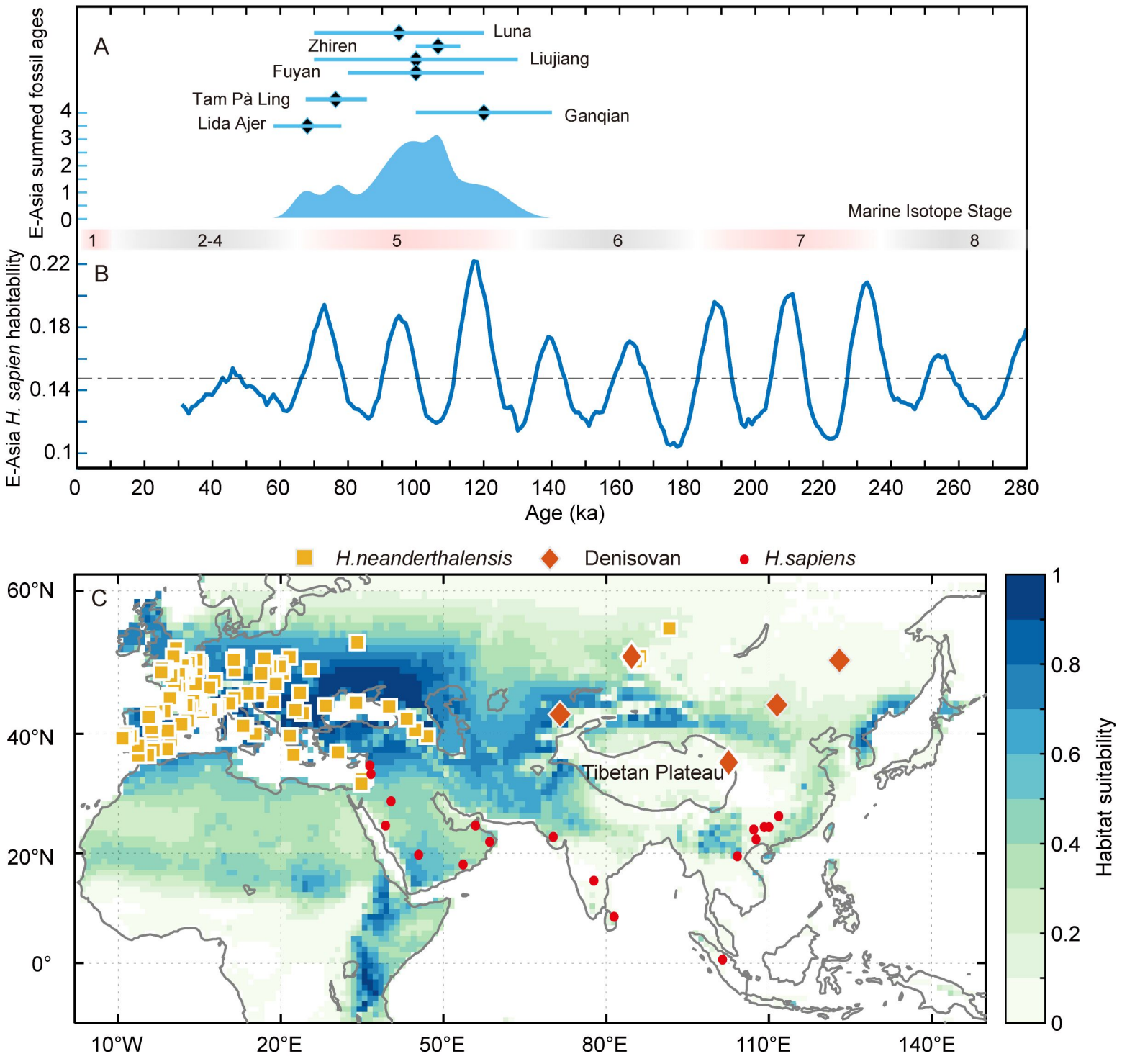
A
Luna
Zhiren
Liujiang
Fuyan
Tam Pà Ling
Ganqian
Lida Ajer
E-Asia summed fossil ages
Marine Isotope Stage
1
2-4
5
6
7
8
B
E-Asia H. sapien habitablity
Age (ka)
H.neanderthalensis
Denisovan
H.sapiens
C
Tibetan Plateau
Habitat suitability